Journal of Materials Chemistry B

RSC**Publishing**

ARTICLE

Rapid, one-pot procedure to synthesise ^{103}Pd:Pd@Au nanoparticles en route for radiosensitisation and radiotherapeutic applications

D. Djoumessi, [† a, b, c] M. Laprise-Pelletier, [† a, b, c] P. Chevallier, [a, b] J. Lagueux [a] , M.F. Côté[a] and M.-A. Fortin*[a, b, c]

† Equal contributors to this work.

The radioisotope palladium (^{103}Pd), encapsulated in millimetre-size seed implants, is widely used in prostate cancer brachytherapy. Gold nanoparticles (Au NPs) distributed in the vicinity of ^{103}Pd radioactive implants, strongly enhance the therapeutic dose of radioactive implants (radiosensitisation effect). A new strategy under development to replace millimetre-size implants, consist in injecting radioactive NPs in the affected tissues. The development of ^{103}Pd@Au NPs distributed in the diseased tissue, could increase the uniformity of treatment (compared with massive seeds), while enhancing the radiotherapeutic dose to the cancer cells (through Au-mediated radiosensitisation effect). To achieve this goal, it is necessary to develop a rapid, efficient, one-pot and easy-to-automatise procedure, allowing the synthesis of core-shell Pd@Au NPs. The novel synthesis route proposed here enables the production of Pd@Au NPs in not more than 4h, in aqueous media, with minimal manipulations, and relying on biocompatible and non-toxic molecules. This rapid multi-step process consists of the preparation of ultra-small Pd NPs by chemical reduction of an aqueous solution of H_2PdCl_4 supplemented with ascorbic acid (AA) as reducing agent and 2, 3-meso-dimercaptosuccinic acid (DMSA) as a capping agent. Pd conversion yields close to 87% were found, indicating the efficiency of the reaction process. Then Pd NPs were used as seeds for the growth of a gold shell (Pd@Au), followed by grafting with polyethylene glycol (PEG) to ensure colloidal stability. Pd@Au-PEG (TEM: 20.2 ± 12.1 nm) formed very stable colloids in saline solution as well as in cell culture medium. The physico-chemical properties of the particles were characterised by FTIR, XPS, and UV-vis. spectroscopies. The viability of PC3 human prostate cancer cells was not affected after a 24-h incubation cycle with Pd@Au-PEG NPs to concentrations up to 4.22 mM Au. Finally, suspensions of Pd@Au-PEG NPs measured in computed tomography (CT) are found to attenuate X-rays more efficiently than commercial Au NPs CT contrast media. A proof-of-concept was performed to demonstrate the possibility synthesise radioactive ^{103}Pd:Pd@Au-PEG NPs. This study reveals the possibility to synthesise Pd@Au NPs rapidly (including radioactive ^{103}Pd:Pd@Au-PEG NPs), and following a methodology that respects all the strict requirements underlying the production of NPs for radiotherapeutic use (rapidity, reaction yield, colloidal stability, NPs concentration, purification).

ARTICLE

1. Introduction

Low-dose rate seed implants are widely used in the treatment of prostate and breast cancers by internal radiotherapy procedures (brachytherapy).[1-4] In such procedures, the permanent seed implants (5 mm) containing low-energy gamma photon emitters, are directly inserted in tumours, where they deliver a radiotherapeutic dose during a prolonged period of time. In this application, the radioisotope ^{103}Pd is widely used. It emits photons with energies of 20.1 keV (64.7%) and 23.0 keV (12.3%), with a half-life of 16.99 days. Because a routine radiotherapeutic treatment necessitates the insertion of tens of seeds per tumour, the placement of each seed is subject to preliminary calculations based on anatomical imaging results (e.g. by computed tomography, CT). In brachytherapy, the dose gradients are very steep; therefore, the dose delivered to tumours falls off sharply with increasing distance from the seed. As a result, the tumour is treated with high doses of radiation while the surrounding normal tissues are not always spared. However, the millimetric seeds are relatively massive compared with the dimensions of the tumour, and their insertion causes discomfort. Therefore, smaller radioactive sources based on injections of nanoparticles (NPs) that could penetrate biological tissues in a less invasive way, and which could distribute more uniformly in the tumour, are being developed. Indeed, injecting NPs at the tumour site could improve the homogeneity of the dose rate delivered to tumours. Such a strategy would also alleviate the inflammation caused by the insertion of many massive radioactive seeds within the same tumour environment. In this context, NPs containing the radioisotope ^{103}Pd would provide a promising technological tool for advanced procedures in prostate and breast cancer radiotherapy.

Gold nanoparticles (Au NPs) have been the subject of intensive research in cancer therapy.[5] For instance, Au NPs are used in diagnostic procedures (with CT) and for therapy (e.g. drug delivery, hyperthermia).[6, 7] Furthermore, Au NPs are biocompatible and their surface can be modified easily with various molecules. Due to their strong photoelectric absorption properties, Au NPs are very efficient CT contrast agents.[5, 8-11] Because Au NPs strongly absorb photons, they have also been used as radiosensitisers in radiotherapeutic procedures.[8, 11, 12] In fact, by distributing Au NPs in tumours prior to radiotherapy, the local dose as well as the homogeneity of radiotherapy response can be considerably improved through the emission photoelectric products (photoelectrons, Auger electrons, characteristics X-rays).[13-15] External beam radiotherapy (250 kV photons) applied to the treatment of tumours containing high concentrations of Au NPs, has proven effective in extending the survival rates of mice.[8, 11] Increased photoelectron emissions during X-ray radiation, resulting in greater damage to cancer cells and to blood vessel endothelial cells in tumours. These promising results have triggered studies aimed at studying the impact of Au NPs size, concentration, intracellular localisation and irradiation energy on the overall radiosensitising effect.[8, 9, 12, 16-18]

To increase the radiosensitisation effect of gold, low-energy photons (< 100 keV) must be used. Indeed, the efficiency of photon capture by the Au NPs is much higher for energies lower than 80.7 keV (k-edge of Au).[19-23] At 20.1 keV, energies corresponding to photons emitted by ^{103}Pd, the mass attenuation coefficient of gold

increases to 78.83 cm^{2}g^{-1} (2.19 and 5.16 cm^{2}g^{-1} at 80 and 100 keV, respectively) and the capture of photons by Au NPs is therefore maximised.[11] However, the penetration of 20 keV-photons in biological tissues is limited, and this rules-out the use of external-beam radiation therapy for deep tumours. For this reason, the insertion of ^{103}Pd (20.1, 23.0 keV photon emitters) directly into the biological tissues to treat, followed by an adequate distribution of gold around the radioactive implants, could enhance the radiotherapeutic treatment through the radiosensitization effect. [16, 23-25] Theoretical studies have demonstrated that Au NPs tumour concentrations in the order of 5 mg Au NPs/g, distributed in the near presence of ^{103}Pd sources, produce massive amounts of photoelectrons and Auger electrons which in turn easily double the dose delivered to soft tissues (compared to conventional external beam therapy).[24] This represents a massive dose of Au NPs, whose direct administration to tumours would necessarily imply certain complications (e.g. inflammatory response). Moderate concentrations of Au NPs (0.1 – 1 mg Au NPs/g; ~ 0.5 – 5 mM Au) could preferentially been used to reach a radiosensitization impact. However, those conditions have never been comprehensively investigated in vivo, using a xenograft tumour model.

As an alternative to conventional millimetre-sized ^{103}Pd brachytherapy sources, the same radioactive dose could be injected in tumours in the form of radioactive NPs. An adequate integration of the radioisotope ^{103}Pd into Au NPs could significantly increase the efficiency of brachytherapy procedures. The synthesis of bimetallic ^{103}Pd:Pd@Au NPs of radiotherapeutic activities (~ 1 mCi per injection), call for the development of rapid, one-pot, high-yield nanoparticle synthesis procedures, relying on biocompatible molecules and performed entirely in aqueous conditions (to avoid tedious solvent exchange procedures, often leaving toxic residues). Until now, few examples of Pd@Au NPs synthesis have been reported in the literature. Those were mainly performed through polyol and thermal decomposition procedures, not in aqueous conditions.[26, 27] The synthesis of radioactive ^{103}Pd-NPs solutions of activities much higher than 10 mCi, requires straightforward manipulations, high conversion yields (Pd ions into Pd NPs), and as few purification steps as possible. Minimizing the manipulation steps is a very important requirement, as each flask or vial transfer step would imply NPs losses, risk of chemical contamination (critical under good manufacturing process – GMP – conditions), and exposure of the manipulators to radioactivity. This rules-out the tedious ligand and solvent exchange procedures characteristics of polyol and thermal decomposition routes, which would also generate excessive radioactive waste (non-reacted ^{103}Pd ions).

In brief, the synthesis of ^{103}Pd:Pd@Au NPs necessitates the development of a protocol performing in aqueous conditions and few manipulation steps. In fact, direct reduction techniques are possibly the most efficient routes to achieve high synthesis yields, and to facilitate manipulation and purification of Au and Pd NPs in aqueous media.[28-31] However, such methods are mainly based on the use of potentially toxic reducing agents,[32] shape-directing additives (e.g. CTAB[33]) as well as organic solvents.[27, 34] For this reason, they do not seem suitable for biomedical applications. Another challenge in direct reduction techniques is the achievement of relatively narrow particle size distributions, which are almost invariably broader than when using the polyol and the thermal reduction routes. Finally,

because the optimal thickness of Au NPs coatings necessary to maximise the radiosensitisation effects, are found in the range 5 to 30 nm, [24] the gold shells surrounding the particles should be relatively uniform and not exceed those values. This adds up to the overall challenge of synthesizing radioactive NPs.

In this study, we report a synthesis procedure that could be advantageously used for the synthesis of therapeutic radioactive NPs. This synthesis enables the rapid production of Pd@Au NPs (and [103]Pd:Pd@Au NPs) in conditions compatible with the requirements of radiochemistry. In this process, ultra-small Pd NPs are first obtained by the chemical reduction of an aqueous solution of H_2PdCl_4 using ascorbic acid (AA) as a reducing agent and 2, 3-meso-dimercaptosuccinic acid (DMSA) as a capping agent. Both molecules are non-toxic and biocompatible. Then, gold shells are grown on the Pd NPs, and the particles are further stabilised by polyethylene glycol (PEG). The physico-chemical properties of the NPs are comprehensively characterised by XPS, FTIR, UV-Vis, and their biocompatibility, studied by cell viability and cell proliferation assays. The potential of Pd@Au-PEG NPs as CT contrast agents is characterised and compared with commercial, Au NPs-based contrast media products. Finally, the possibility to synthesize radioactive [103]Pd:Pd@Au-PEG NPs with such procedure, is demonstrated.

2. Experimental

2.1 Chemicals

Palladium chloride ($PdCl_2$ ≥99.9% trace metals basis), L-ascorbic acid (AA), 2, 3-meso-dimercaptosuccinic acid (DMSA), sodium hydroxide and nitric acid were purchased from Sigma-Aldrich (Oakville, ON, Canada). Hydrochloric acid (37%) was obtained from Fisher (Canada). NH$_2$-PEG-SH (5000 Mw) was obtained from Laysan BIO (Arab, AL, USA). Nanopure water (18.2MΩ·cm) produced by a Barnstead ultrapure system was used in all experiments. All glassware and magnetic stir bars were cleaned with aqua regia (HCl and HNO_3 in a 3:1 volumetric ratio) and thoroughly rinsed with nanopure water before use. Radioactive [103]Pd in the form of palladium chloride in dilute ammonium hydroxide (500 mCi/mL; half-life [103]Pd: 16.99 days; pH 11) was ordered from Nordion (Vancouver, Canada).

2.2 Synthesis of Pd NPs

To synthesise the small Pd cores for the Pd@Au nanoparticles, tetrachloropalladinic acid (H_2PdCl_4) was used as a precursor. H_2PdCl_4 was obtained by dissolving 26.5 mg of $PdCl_2$ in HCl solution (3 mL, 50 mM), then the final volume of the solution was adjusted to 150 mL with nanopure water. DMSA was mixed with a 2 mM aqueous solution of sodium hydroxide (NaOH) before use. As a first step, the synthesis of Pd NPs cores was performed according to the following preparation variants (S1–S3):

S1. H_2PdCl_4 (5 mL, 1 mM) was added under constant stirring to a mixture containing a freshly prepared aqueous solution of AA (0.5 mL, 0.1 M) and DMSA (1 mL, 1 mM). The solution turned from light yellow to dark brown within 5 min. indicating the formation of Pd NPs. The mixture was stirred at room temperature (RT) for about 15 min, and then purified before characterisation.
S2. The solution of AA was added to a mixture containing H_2PdCl_4 and DMSA. The solution turned from light yellow to

orange then to dark brown within 15 min. The resulting mixture was stirred at RT for another 15 min.
S3. AA was directly mixed with H_2PdCl_4 followed by the addition of DMSA. The solution turned from light yellow to dark brown within a few seconds after the addition of AA. The resulting solution was stirred for 15 min at RT.

For transmission electron microscopy (TEM), X-ray photoelectron (XPS) and Fourier-transform infrared (FTIR) spectroscopy analyses, Pd (S1-S3) and Pd@Au-PEG NPs were purified by dialysis in nanopure water for 28h, to eliminate free ions and excess reagents. A membrane pore size of 3500 MW and 10000 MW (Spectra/Por#6, Rancho Dominguez, CA, USA) was used for Pd and Pd@Au-PEG NPs, respectively. During the dialysis process, the water was changed five times.

2.3 Gold coating procedure leading to Pd@Au NPs

Pd NPs solutions from S1, having shown a mean diameter size close to 10 nm (TEM results, Fig. 2), were coated with a gold shell. For this, 0.5 mL of an aqueous solution of $HAuCl_4$ (10 mM) was injected under vigorous stirring to 0.5 mL of as-synthesised Pd NPs (S1), 1 mL of ascorbic acid (0.1 M), and 5 mL of nanopure water. The solution was stirred for 5 min before the addition of 6.5 mL of stabilising agent (NH$_2$-PEG-SH, 2 mg/mL) aqueous solution. The resulting mixture was adjusted to 15 mL with nanopure water. Finally, the solution was left under stirring at RT for about 2h before purification and characterisation.

2.4 Synthesis of radioactive [103]Pd:Pd@Au NPs

The synthesis of radioactive [103]Pd:Pd@Au NPs was performed first by the production of ultra-small Pd cores, using a variant of the "S1" synthesis. For this, a solution of H_2PdCl_4 was prepared by diluting 0.5 mM of $PdCl_2$ in HCl (3 mL, 100 mM) followed by addition of nanopure water (147 mL). The solution was stirred overnight until complete dissolution of $PdCl_2$. For the DMSA solution (1 mM), optimal results (ultra-small particle sizes) were obtained when using solutions aged at least 4 days. Due to rapid oxidation, ascorbic acid solutions were always freshly prepared (0.1 M, prepared < 2h before synthesis).

In a 1.5 mL-tube, one (1) μL of [103]$PdCl_2$ (700 μCi; [03]$PdCl_2$), was mixed with 500 μL of the H_2PdCl_4 solution. In another 1.5-mL tube, 200 μL of the DMSA solution as mixed with 100 μL of the AA solution; the [103]$PdCl_2$ mixture was added to this tube, and carefully re-suspended. The colour turned from light yellow to deep brown, indicating the synthesis of ultra-small Pd cores (similar to that observed in S1). This procedure (instantaneous reaction) was repeated several times in small volumes to minimize heterogeneity in the reaction. In the end, the samples were pooled (24 mL; total activity: 21 mCi). The hydrodynamic size of the pooled [103]Pd:Pd NPs was measured in DLS (d = 13.3 nm, number- weighted; d = 30.4, intensity-weighted; DLS measurement detailed in section 2.5).

For the Au coating, 4 mL aliquots of the [103]Pd:Pd NPs suspension were dispersed in 6 tubes (total volume of NP suspension: 24 mL). In each tube, 12.5 mL of nanopure water was first added, followed by 0.8 mL of $HAuCl_4$ solution (0.1 M) and two successive additions (0.64 mL and 0.4 mL, respectively) of AA (0.1 M). To confirm the Au coating, the hydrodynamic diameter of the [103]Pd:Pd@Au NPs was measured in DLS (d = 29.6 nm, number-weighted; d = 56.9,

intensity-weighted). Then, the stabilizing PEG solution was added in each tube (1.875 mL; 10 mg/mL), followed by pipette agitation (several ups and downs). The mixture was left ~2h for reaction with the gold surface. To remove the free metal ions and excess PEG from the suspension, ^{103}Pd:Pd@Au-PEG NPs were centrifuged (16000g, 15 min.) and resuspended in ultra-pure water (1:20 volume ratio). This cycle was repeated thrice; after each centrifugation, the supernatant was collected and radioactivity-counted (see details in section 2.10). The final nanoparticle suspension (125 µL), very dense and too viscous to be efficiently pipetted, was adjusted to 600 µL, and radioactivity-counted.

2.5 Particle size analysis

DLS: The hydrodynamic diameter of aqueous suspensions of Pd (S1-S3) and Pd@Au-PEG NPs were measured by dynamic light scattering (DLS) with a Nano S Zetasizer system (Malvern Instruments, Worcestershire, UK.) using a laser (He-Ne) wavelength of 633 nm and a scattering angle of 173°. The temperature measurement was fixed at 25° C. The viscosity and the refractive index of water were set to 0.8872 cp and 1.33. For Pd NPs, the refractive index was set to 1.80 while for Pd@Au-PEG NPs the refractive index was set to 0.20. The hydrodynamic diameter was calculated from the average of three measurements. The polydispersity index (PdI, i.e. the square of the standard deviation of NP/ mean NP diameter) was calculated using the Malvern Zetasizer software.

TEM: The NPs were also visualised using a FEI TECNAI Spirit Biotwin (FEI Company, USA) transmission electron microscope (TEM) operating at an accelerating voltage of 120 kV. Drops of the NPs suspensions were deposited on carbon-coated copper grids. Size-distributions were extracted from the TEM images (on at least 150 NPs) and the mean diameters of particles were measured using the Image J software (version 1.49d; Wayne Rasband, National Institutes of Health, USA). To demonstrate and characterise the core-shell nature of Pd@Au-PEG NPs, high-resolution images and energy-dispersive spectroscopy (EDS) data were acquired on a Jeol JEM-2100F operating at an accelerating voltage of 200 keV.

2.6 Physico-chemical characterisation

UV-visible spectroscopy: UV-visible spectra of NPs solutions were acquired with a Shimadzu UV-1601 spectrophotometer over the spectral range 250-1000 nm, using a quartz cell.
FTIR analyses: drops of the NPs suspensions were dried on a Si crystal, and measured with an ATR-FTIR (Agilent Cary 660 FTIR, Agilent technologies, USA), equipped with a deuterated L-alanine-doped triglycine sulfate (DLa-TGS) detector and a Ge-coated KBr beam splitter.
XPS: Pd and Pd@Au-PEG NPs as well as starting products were characterised by XPS (PHI 5600-ci spectrometer, Physical Electronics U.S.A., MN, USA). Samples of particles were deposited and dried on silicon substrates previously cleaned by TL2 and TL1 solutions (TL2 solution, a mixture of nanopure water, 30% hydrogen peroxide (H_2O_2, Fluka, ON, Canada) and concentrated hydrochloric acid (HCl, Fisher, Canada) (6:1:1), at 80°C for 10 min and TL1 solution, a mixture of nanopure water, 30% H_2O_2 and 25% ammonia (Fisher, IL, USA) (5:1:1), at 80°C for 10 min). The wafers were thoroughly rinsed with nanopure water and anhydrous ethanol and quickly dried under medical air. Pd and Pd@Au-PEG NPs were deposited on these substrates and analysed by XPS using a standard aluminium X-ray source for survey spectra (0-1400eV) while high-resolution

(HRXPS) spectra of C1s, O1s, S2p, Pd 3d, Au 4f and N1s were obtained using a standard magnesium X-ray source (1253.6 eV). Charge neutralisation was not applied for either analysis. The detection was performed at 45° with respect to the surface normal and the analysed area was 0.005 cm^2. The spectrometer work function was adjusted to give 285.0 eV for the main C (1s) peak. Curve fittings for high-resolution peaks were determined by means of the least squares minimisation procedure employing Gaussian-Lorentzian functions and a Shirley-type background.

2.7 Elemental analysis

Samples of the dialysed S1 solution, as well as the dialysed Pd@Au-PEG final solution were digested in aqua regia (HCl and HNO$_3$ in a 3:1 volumetric ratio + H_2O_2 (30%, Sigma Aldrich) at 115°C, until the suspension turned clear and transparent. Au and Pd concentrations were measured by atomic absorption spectroscopy (AAS, Perkin Elmer Analyst 800).

2.8 Cell viability and cell proliferation assays

The viability of human PC3 prostate cancer cells (CRL-1435, American Type Culture Collection, Manassas, USA) after exposure to concentrated solutions of Pd@Au-PEG was measured by the trypan blue assay. For this, 6000 PC-3 cells were seeded in 96-well plates and incubated for 24h (37°C, 5% CO$_2$). Then, the cells were washed twice with Dulbecco's Modified Eagle Medium (DMEM, Life Technologies, Burlington, ON, Canada). The cells were incubated in triplicate with different concentrations of Pd@Au-PEG NPs (0.5, 1, 2 and 10% v/v, corresponding to 0.211, 0.422, 0.844, and 4.22 mM Au, respectively. In the more concentrated wells (4.22 mM), the colour of the culture medium was dark red, reflecting the high concentration of NPs. The total volume of fluid per well was kept to 200 µL. After 24h, the culture medium was removed and the cells were rinsed three times with DMEM. Trypsin-EDTA (0.5%, concentrated 10X, Life Technologies, Burlington, ON) was used to harvest the cells (50 µL/well, 37°C, 5 min). A 150 µL/well aliquot of complete culture medium was used to resuspend the cells, followed by 5 min of centrifugation at 390 g. Finally, the cells were resuspended in 200 µL of culture media, and 20 µL of this suspension was mixed with 10 µL of trypan blue (0.4% w/v, Sigma-Aldrich, Oakville, ON, Canada), followed by hemacytometer counting. The percentage of viable cells was calculated by dividing the number of viable cells in the harvested well, by the number of viable cells in control wells (cell not treated with Pd@Au-PEG NPs).

Cell proliferation measurements were performed using the sulforhodamine-B (SRB) colorimetric assay based on the measurement of cellular protein content. For this, 2000 cells/well were seeded in a 96-well plate and incubated for 24h (37°C, 5% CO$_2$). Then, the cells were incubated with the same concentrations of Pd@Au-PEG NPs as for the cell viability test (in triplicate). The total volume of fluid per well was kept to 200 µL. After 24h, the incubation solutions were removed and each well was rinsed twice with fresh complete culture medium. 200 µL of complete culture medium was added in each well and the incubation was prolonged to 48h. The supernatant was discarded and the cells were washed twice with complete culture medium. Assays were stopped by addition of

cold trichloracetic acid (Amresco, Solon, OH, USA) to a final concentration of 10% v/v followed by incubation for 60 min at 4°C. The supernatant was discarded; the plates were washed five times with tap water, and air-dried. SRB solution (50 µL at 0.1% w/v in 1% acetic acid, Sigma-Aldrich, Oakville, ON, Canada) was added to each well and plates were incubated for 15 min at RT. After staining, unbound dye was removed by washing five times with 1% acetic acid, and the plates were air-dried. The bound stain was solubilised with 10 mM of Tris base (Amresco, Solon, OH, USA) and the optical density was read at 545 nm using a µQuant Universal Microplate Spectrophotometer (Biotek, Winooski, VT, USA). Cell proliferation results were plotted based on the calculation of the ratio between optical density of treated cells, and optical density in controls (untreated cells).

2.9 X-ray attenuation measurements

Pd@Au-PEG NPs and AuroVist™-15 nm (Nanoprobes, Yaphank, NY, USA) in different concentrations (10.5, 21.1, 31.6 and 42.2 mM of Au), were placed in 0.2 mL Eppendorf tubes. The tubes were positioned in a holder, and immersed in nanopure water prior to CT scanning (eXplore Locus 80, GE Healthcare Technologies, Milwaukee, WI). The scans were performed at 40, 60 and 80 kV (current: 450 µA). The detector exposure time was 90 ms, detector binning was 4x4 for a voxel resolution of 89 µm with 3 frames averaging. Image reconstruction was performed using the Parallax Innovations Reconstruction tool from Parallax Innovations (Ilderton, ON, Canada). A standard Hounsfield unit (HU) calibration was performed at each X-Ray energy. Image analysis was performed using Image J software processing (version 1.49d; Wayne Rasband, National Institutes of Health, USA).

2.10 Radioactivity counting

^{103}Pd:Pd@Au-PEG NPs radioactivity measurements where performed using an Atomlab 100 dose calibrator (Biodex Medical systems, Shirley, NY). ^{103}Pd is a non-standard isotope, a specific calibration value (supplied by the manufacturer) was programmed based on a calibration curve. In brief, 1.1 µL (1 mCi; calibration date of the ^{103}PdCl$_2$ solution from MDS Nordion) of the ^{103}PdCl$_2$ solution was diluted in nanopure water to yield 1000, 400, 250, 100, and 10 µCi standards. These standards were measured in the dose calibrator, and the results were plotted against the theoretical activities to provide a calibration curve. A linear regression equation was

calculated (R^2 = 0,99979) and the calculated correction factor (1.88) applied to all activity measurements performed in the dose calibrator. Finally, aliquots of ^{103}Pd:Pd@Au-PEG were visualized in CT as well as in single photon emission computed tomography (SPECT; Philips Brightview; static scan; energy window: 18 ± 7 keV; magnification: 2.1 x 256 x 256; 30 min.).

3 Results and discussion

The synthesis of ultra-small cores of Pd has been reported in the literature, based on polyol synthesis,[35, 36] thermal decomposition,[37-40] and direct reduction methodologies.[28-30, 41] Most of these studies were oriented toward catalytic applications [42-44] and sensor devices.[45, 46]

The direct reduction route that was developed in this study makes use of biocompatible molecules (AA DMSA), enabling the synthesis of Pd and Pd@Au NPs. AA was used as the reducing agent, and DMSA as the stabilising agent, respectively. Changing the addition order of reactants modulated the size of Pd NPs. These Pd NPs were used as seeds for the preparation of Pd@Au NPs. The final Pd@Au NPs were capped with amine-PEG-thiol, a protective biocompatible molecule preventing aggregation in high salinity conditions, and preventing protein adsorption in physiological fluids.

3.1 Synthesis of Pd (S1-S3) NPs

Pd NPs were obtained from the chemical reduction of palladium chloride by ascorbic acid in water, in presence of DMSA as a surface ligand. The nucleation and growth of Pd NPs occurred within a few minutes and was visually confirmed by a strong colour change from yellowish (for the H$_2$PdCl$_4$ solution) to dark brown (for the Pd NPs solution) for the three syntheses variants. The reduction of palladium salt into Pd NPs was also confirmed by UV-vis spectroscopy (Fig. 1a-d). Indeed, before reduction, the precursor H$_2$PdCl$_4$ solution exhibited two UV-Vis peaks at 420 nm and 305 nm, attributed to metal-ligand charge transfer.[30, 47] Because Pd^{2+} ions were reduced in Pd^0, the bands do not appear in S1-S3 (Fig. 1b-d). The formation of a nanoparticle suspension is clearly indicated by the increased background. .
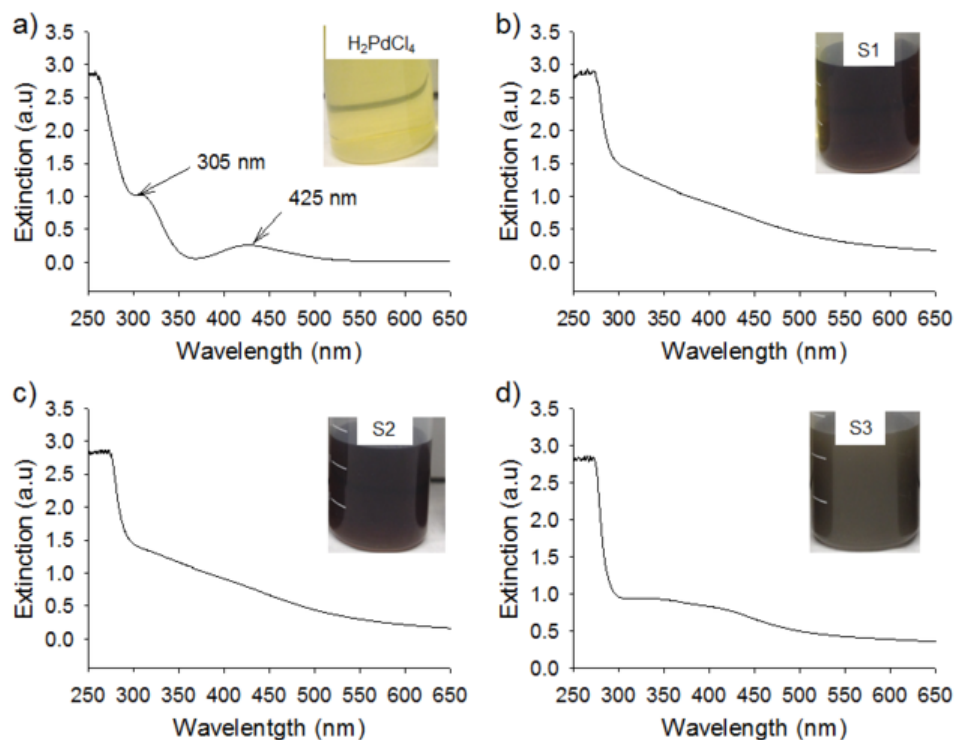
Fig. 1 UV-Visible spectra of (a) palladium precursor solution and (b-d) Pd nanoparticle solutions (S1-S3); images of the solutions are provided as inserts.

3.2 Pd NPs size study

Compared with polyol and thermal decomposition techniques, direct reduction is, in general, associated with broader NPs size distributions. In the present case, relatively narrow particle size distributions were achieved in S1 and S2. The TEM nanoparticle size study (Fig. 2a, 2d and 2g) revealed ultra-small NPs nearly spherical in shape (mean diameters: 9.3 ± 4.8 nm for S1; 7.5 ± 3.6 nm for S2). Much larger NPs with a mean size of 114.4 ± 27.7 nm were obtained in the case of S3. Furthermore, S2 (Fig. 2e) demonstrated the smallest and narrowest size distribution profile. The difference between NPs size can be explained by the fact that the reducing power of AA depends on the pH value of the reaction medium. Indeed, the reduction power of AA was typically enhanced at higher pH value.[48-50] Hence when AA was used in an acidic medium (H_2PdCl_4, pH 2-3) followed by DMSA addition (pH 5-6), AA promoted the rapid growth of particles. This may have induced the fusion of a certain fraction of primary NPs at the particle growth step (S3). However, when H_2PdCl_4 was added to a mixture containing AA (pH 2.5) and DMSA (S1), or when adding AA to a solution of H_2PdCl_4 and DMSA (S2), the nucleation of a large number of small clusters, followed by nanoparticle growth, occurred.

As expected, hydrodynamic diameters larger than the particle size measured by TEM were found in all of the Pd NPs samples (Fig. 2c, 2f and 2i). This observation is in agreement with the presence of DMSA at the surface of particles. Intensity-weighted hydrodynamic diameters of 29.8 nm (18.1 nm in number), 18.6 nm (9.7 nm in number) and 108 nm (61.3 nm in number) were found for S1, S2 and S3 respectively. Overall, DLS measurements demonstrated a good size distribution (polydispersity index < 0.3) without evidence of large clusters or aggregates, except for S2. Because of the presence of this contribution, S2 was discarded from subsequent Au coating procedures.

This one-pot process led to the rapid and high-yield synthesis of Pd NPs. The conversion yield of Pd^{2+} to Pd^0 was estimated by AAS. For this, 1 mL of as-dialysed S1 solution was digested in aqua-regia (as described in 2.6), and measured in AAS (0.8663 mM of Pd). Considering that 1mM of palladium salt was used for the synthesis of S1 NPs, and that no observable volume change was noted during the dialysis, the estimated yield of the reaction calculated from these values was

at least 87 %. In fact, the yield is most probably higher taking into account the NPs losses on the dialysis membrane.

High zeta potentials were found for all three S1-S3 suspensions (at pH 5-6: -42.5, -38.2 and -47.5 mV, respectively). The anionic charge of the particles conferred a strong electrostatic repulsion to the colloidal suspension. This was further confirmed by colloidal stability tests, which have evidenced that S1-S3 NPs suspensions were very stable for several weeks at room temperature without any sign of

aggregation. Furthermore, the suspensions were stable for at least 4 months when kept at low temperatures (4-8°C).
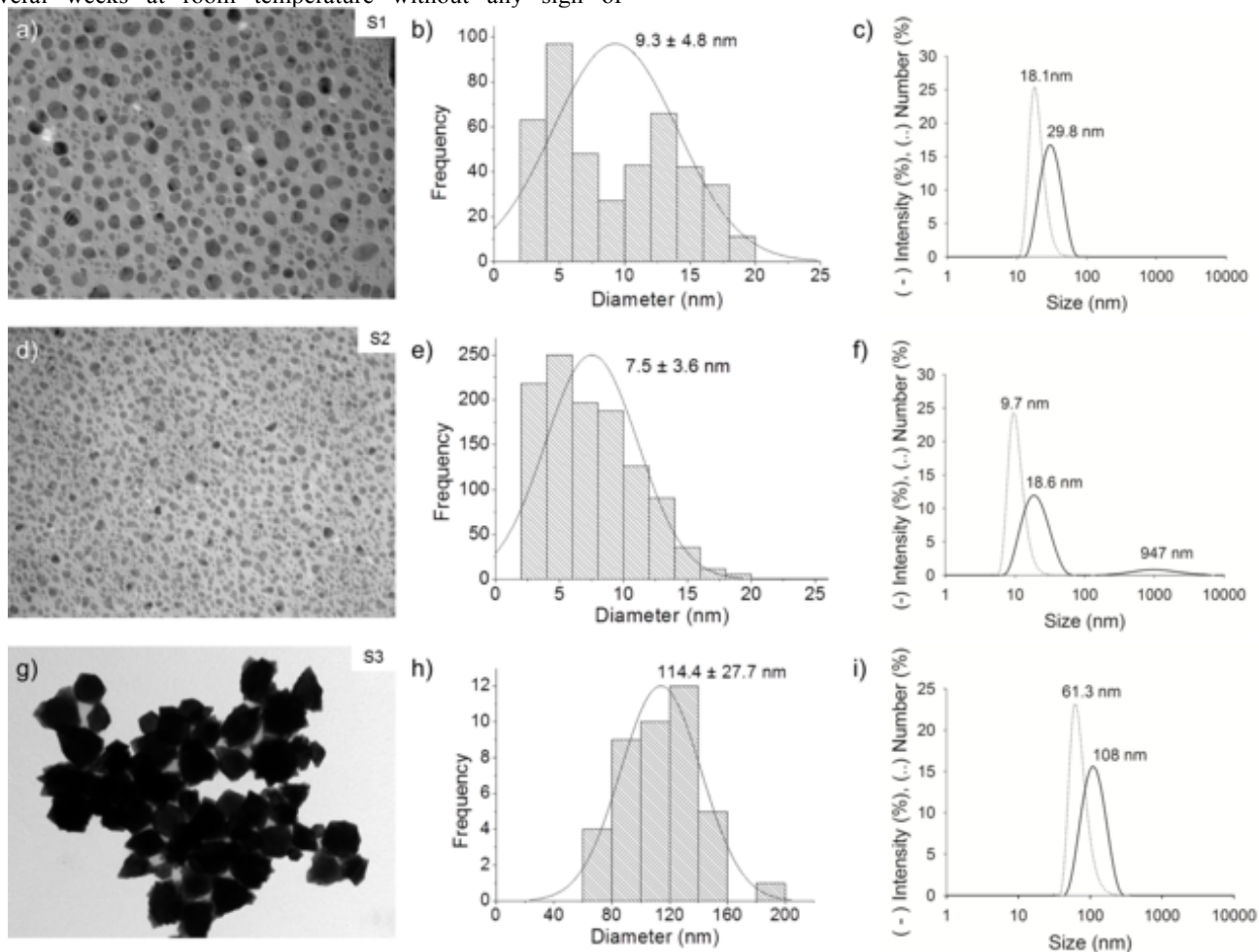
Fig. 2 TEM images, size distribution and hydrodynamic diameters of S1 (a-c), S2 (d-f) and S3 (g-i) NPs.

3.3 Physico-chemical analysis of S1-S3 NPs surface

FTIR spectra of AA, DMSA and as-prepared Pd NPs are presented in Fig. 3. S1, S2 and S3 NPs clearly exhibited different spectra compared to AA and DMSA. On NPs-related spectra, the main band characteristics of both AA and DMSA, are either absent or strongly shifted. Indeed, the vibration of C=C and C=O (lactone) detected on AA spectra at 1658 cm^{-1} and 1749 cm^{-1} respectively, as well as the C=O vibrations of DMSA carboxylic groups at 1695 cm^{-1}, were no more visible in the S1-S3 spectra. This reveals a change in the chemical environments of these specific functions of AA and DMSA, throughout the NPs synthesis process. In the S1-S3 NPs spectra, two new broad bands appeared at 1600 cm^{-1} and 1360 cm^{-1}. These bands, much higher in the case of S2 and S3, are associated to the antisymmetric and symmetric vibrations of carboxylate groups upon chelation with Pd NPs. The frequency

difference between these two vibrations (Δv) is associated to the binding type between the carboxylate groups and the metal:

for $\Delta v \leq 110$ cm^{-1}, the coordination is bidentate; for $\Delta v \geq 200$ cm^{-1}, it is monodentate; between these values, the coordination is bridging. [51, 52] In the S1-S3 Pd NPs, a difference of more than 200 cm^{-1} is observed (monodentate).

In this chelation process, it is difficult to extract the respective contribution of the carboxylic groups in DMSA, to that from AA. During the reduction step of Pd^{2+}, AA is oxidised into dehydroascorbic acid (DHA), as evidenced by the disappearance of the C=C vibration at 1658 cm^{-1}. However, the AA can further hydrolyse, to form 2,3-diketogulonic acid (2,3-DKG) with a terminal free carboxylic group.[53] This degradation leads to the attenuation of the vibration band of lactone (C-O-C, expected at 1025 cm^{-1}); this was precisely the case in S2-S3 spectra). This attenuation effect was very strong for S1 and moderate for S2 and S3. This is an indication of the relatively

strong residual presence of AA at the surface of S2 and S3 NPs. This observation was also confirmed by the attenuated bands at 1360 cm^{-1} (symmetric vibrations of chelated carboxylate groups) in S1 compared to S2-S3.

Further information on the NPs surfaces was revealed by XPS. The results are summarised in Table 1 and in Fig. 4. Similar elemental compositions were found for S2 and S3. For instance, the relative fraction of Pd was 10 times lower in S2 and S3 NPs, compared to S1 NPs. Because XPS is a surface analysis technique (~5 nm depth), this information reveals the presence of thicker coatings on S2-S3 NPs. Higher carbon contents in S2 and S3, were attributed to residual AA, as indicated by FTIR results. Lower sulphur contents in S2-S3 NPs, confirmed that the higher relative carbon observed in S2-S3, could be attributed to AA rather than DMSA. Indeed, S1 NPs exhibited a C/S ratio closer to the DMSA structure (3.3 for S1, and 2.6 for DMSA). Finally, the Pd/S ratio was 4 times higher on S1 than for S2-S3 NPs, further confirmed the stronger presence of DMSA (and not AA), at the surface of S1.

Not only has the synthesis process a clear influence on the size (TEM and DLS, Fig. 2) but also on the coating composition, as revealed by FTIR and XPS analyses. High-resolution XPS spectra were performed on the Pd 3d$_{5/2}$ peaks (Fig. 4a-c). Indeed, Pd 3d$_{5/2}$ of S1 NPs are characterised by two peaks: the first peak at 336.3 eV can be attributed to the metallic specie (Pd^0), while the second peak (337.8 eV) is generally associated to oxidised Pd.[30, 54, 55] The deconvolution of Pd 3d$_{5/2}$ in S3 and S2 NPs, revealed only one peak around 337 eV (between Pd^0 and Pd). The observed shift was attributed to the same ligand configuration that led to the FTIR bands at 1600 and 1360 cm^{-1}, corresponding to the antisymmetric and symmetric vibrations of carboxylate groups upon chelation with Pd NPs. Indeed, changes in the charge density around the Pd specie, result in a shift to higher energy values ($\Delta = 0.9$ eV).
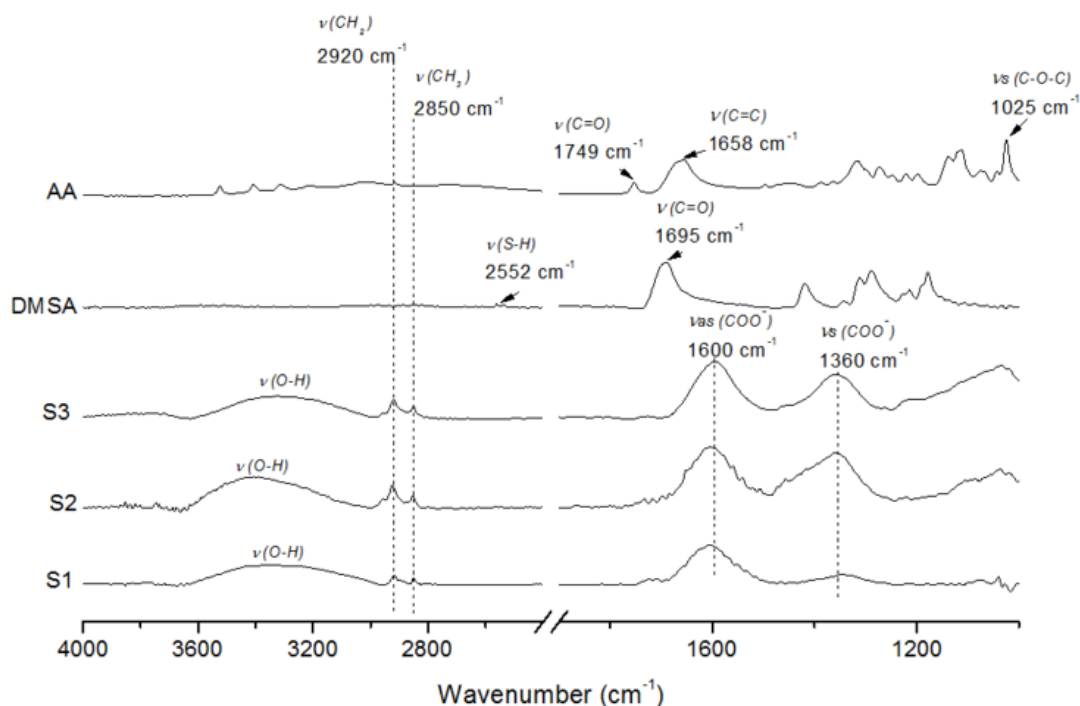

Fig. 3 FTIR spectra of AA, DMSA and Pd NPs (S1- S3).

Table 1 Chemical composition of Pd NPs assessed by XPS analysis*

Sample	% C (285.0 eV : C-C/C-H) [286.5 eV: C-O] {288.9 eV: C=O}	% O**	% S (162-164 eV : S-H) [167-169 eV: S-S]	% Pd	C/S	Pd/S
S1	29.8 (19.4) [6.9] {3.5}	43.1	9.0 (7.7) [1.3]	18.1	3.3	2.0
S2	41.7 (33.0) [5.4] {3.3}	34.7	3.2 (2.1) [1.1]	1.9	13.0	0.6
S3	46.2 (36.5) [6.5] {3.2}	29.1	5.9 (3.8) [2.1]	1.6	7.9	0.3
DMSA [56]	43.9	39.0	17.2		2.6	

* The balance in XPS for S1-S3 nanoparticles were Si, Na and Cl;

** O1s deconvolution is impossible due to the overlap with the Pd3p peak. Here, the oxygen concentration was estimated by subtracting from the O1s peak, the contribution of Pd3p estimated from the Pd3d5/2 peak. The respective sensitivity factor of each peak was also taken into account.
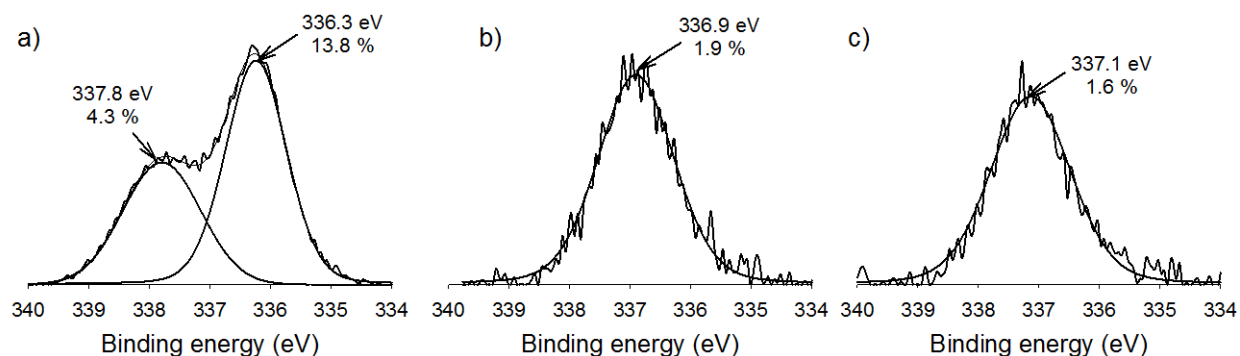
Fig. 4 Pd 3d and high-resolution XPS spectra of S1 (a), S2 (b) and S3 (c).

3.4 Pd-Au NPs synthesis

After synthesis of the small, DMSA-coated Pd nanocores, the second step consisted in covering the NPs with a gold layer (Fig. 5a) in order to obtain Pd@Au NPs with an average size in the range 20-50 nm (optimal radiosensitisation potential). [24] To achieve this goal, the S1 NPs synthesis procedure appeared optimal, due to thinner DMSA coatings, higher contents in metallic palladium (Pd^0), and small Pd NPs cores. Indeed, Pd NPs solution from S3 were too large (d = 114.4 nm), and S2 NPs, despite exhibiting the smallest NPs size (d = 7.5 nm), showed a certain degree of agglomeration (Fig. 2.f). The Pd@Au core-shell NPs were obtained by reducing $HAuCl_4$ at the Pd NPs surface, a process that takes place in a few minutes only (schematic representation Fig. 5a). In this process, AA was used as reducing agent while NH_2-PEG-SH was used as a stabilising agent. Upon reaction, the colour of the Pd NPs suspension rapidly changed from clear brown to dark red, which clearly indicated the deposition of a gold shell on S1 Pd NPs as confirmed in UV-Visible spectroscopy (Fig. 5d, strong plasmon band at 530 nm).

3.5 Pd@Au NPs size study

TEM imaging (Fig. 5b) and size distribution (Fig. 5c) of Pd@Au-PEG NPs indicated the formation of spherical NPs with a mean diameter of 20.2 ± 12.1 nm. The presence of a gold shell on S1 NPs was further confirmed by HRTEM and EDX analysis (Fig. 7). DLS measurements clearly evidenced the presence of PEG at the NPs surface (hydrodynamic diameters of 69.9 nm in intensity and 38.9 nm in number, respectively; Fig. 8a-b). A polydispersity index < 0.3 was found, without any evidence of aggregation. The zeta potential of these NPs shifted

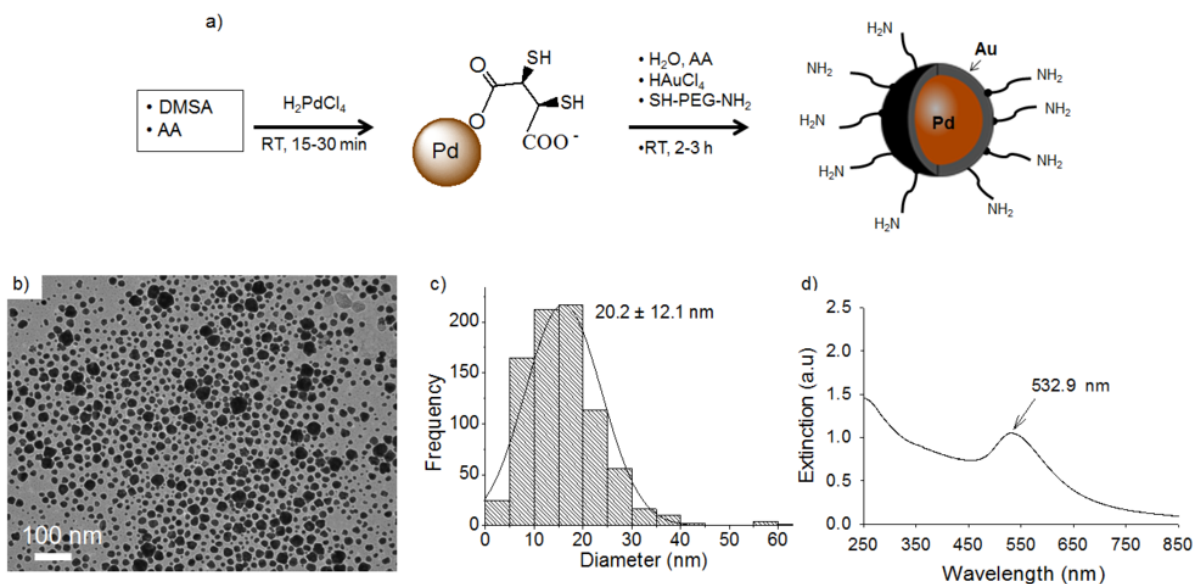from strongly negative (for DMSA-coated Pd NPs cores) to moderate positive values (+ 10.9 mV at pH 5-6).

Fig. 5   Reactive scheme of the one-pot Pd@Au-PEG NPs synthesis process (a). TEM image (b), size distribution (c) and UV-visible spectrum (d).

3.6 Physico-chemical analysis of Pd@Au-PEG NPs surface

The presence of PEG on the Pd@Au NPs surface was confirmed by FTIR (Fig. 6a). Indeed, the broad bands at 1600 and 1360 cm^{-1}, characteristic of the carboxylate vibrations in S1 Pd NPs, were no longer detected. Instead, the C-O-C vibration band at 1103 cm^{-1}, characteristic of the PEG structure, became predominant in Pd@Au-PEG NPs. The PEG grafting efficiency was also evidenced by the peak at 2880 cm^{-1}, assigned to CH_2 vibration, as well as by the band at 1460 cm^{-1} corresponding to NH_2 stretching. XPS analyses (Table 2) confirmed the strong presence of both the gold shell (Au: 13.5%) and the PEG coating (63.3% C). High-resolution spectra (Fig. 6b-c) revealed

the strong C-O band at 286.5 eV, associated to the PEG structure. Furthermore, the Au4f high-resolution spectra of the as-prepared Pd@Au-PEG NPs revealed four contributions (Fig. 6d). The main contribution of Au $4f_{5/2}$ and Au $4f_{7/2}$ appeared at 87.3 and 83.6 eV, respectively. It was ascribed to Au^0. Smaller peaks at higher energies were attributed to the chemical link between thiol groups from HS-PEG-NH_2, and gold (Au-S). No contribution of Pd was observed on the Pd@Au-PEG NPs, indicating the encapsulation of Pd NPs in a thick Au-PEG coating. This observation was also confirmed by energy dispersive spectrometry (EDS) which showed a predominant Pd signal in the core of the particles, and much higher Au signal in the shell (Fig. 7).
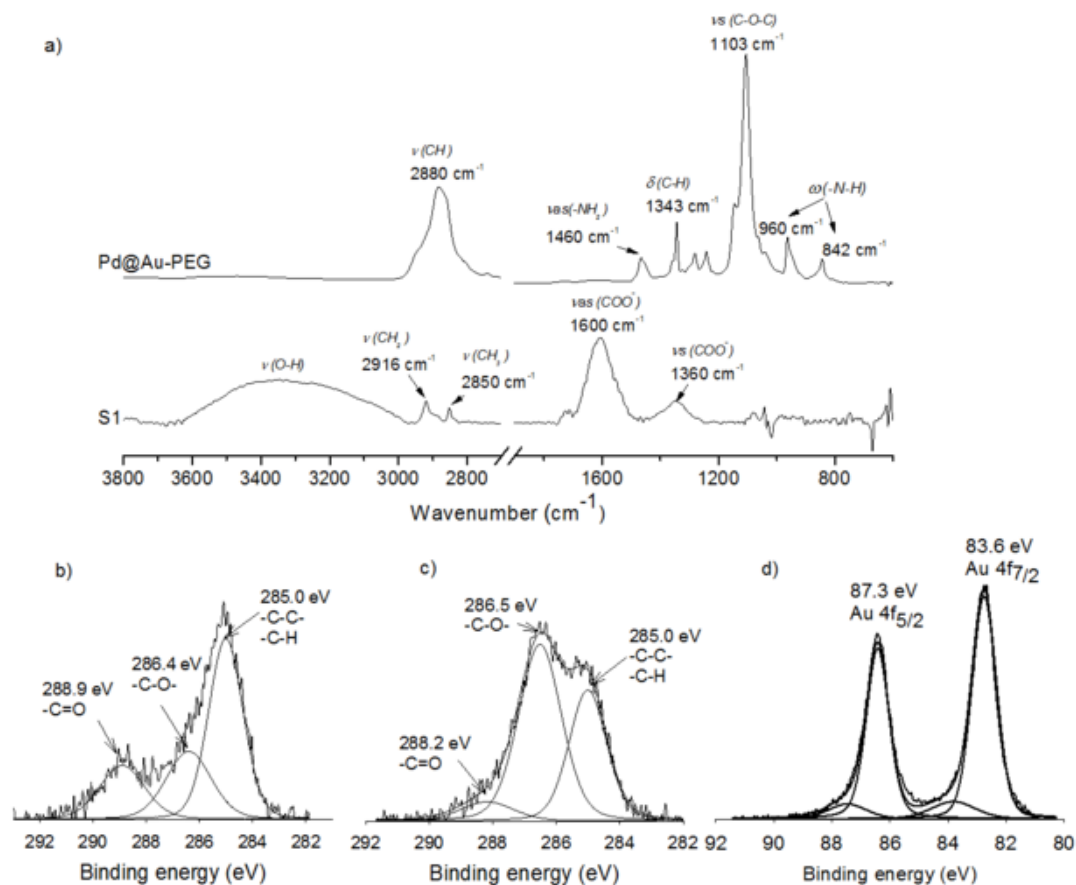
Fig. 6 FTIR spectra of Pd (S1) and Pd@Au-PEG NPs (a); C 1s high-resolution XPS spectra of S1 (b); Pd@Au-PEG NPs (c) and Au 4f high resolution XPS spectrum of Pd@Au-PEG NPs (d).

Table 2 Elemental composition of Pd@Au-PEG NPs

Sample	% C	% O	% S	% Pd	% N	% Au
Pd@Au-PEG	63.3	23.2	0	0	0	13.5
NH$_2$-PEG-SH	65.9	33.5	0.3	-	0.3	-
S1	29.8	43.1	9.0	18.1	-	-
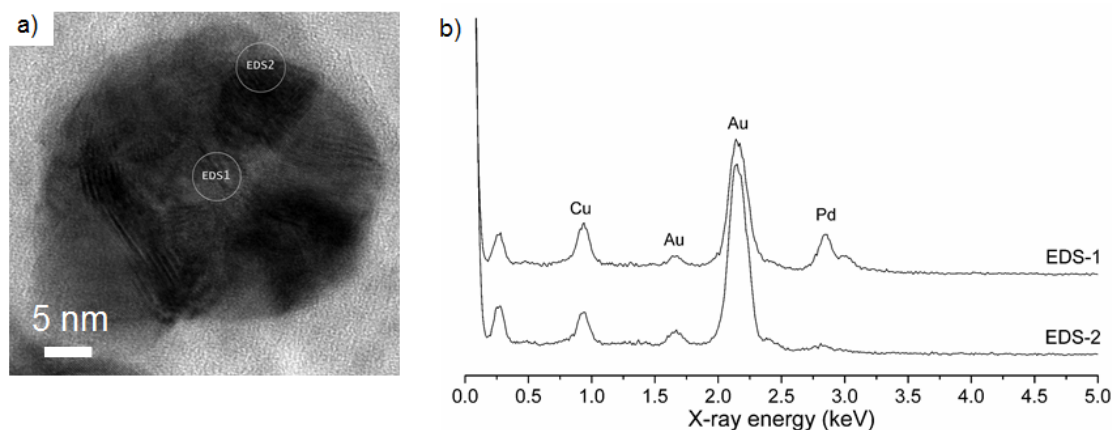
Fig. 7 HRTEM image (a) and EDS spectra of Pd@Au-PEG NPs (b).

3.7 Pd@Au NPs *in vitro* colloidal stability assays

For *in vivo* application as well as for storage purposes, Pd@Au-PEG NPs must remain as a stable colloid when submitted to physiological fluids. Colloidal stability was assessed in cell culture medium and in saline solutions (154 mM NaCl) for up to 7 days. No sign of aggregation was observed after 7 days in saline (Fig. 8a-b), which confirmed the strong stabilising contribution of PEG. Pd@Au-PEG NPs (2% and 10% v/v) suspended in complete DMEM cell culture media revealed slightly increased hydrodynamic sizes, without evidence of aggregation. The size increase was attributed to the formation of a protein corona around the NPs.
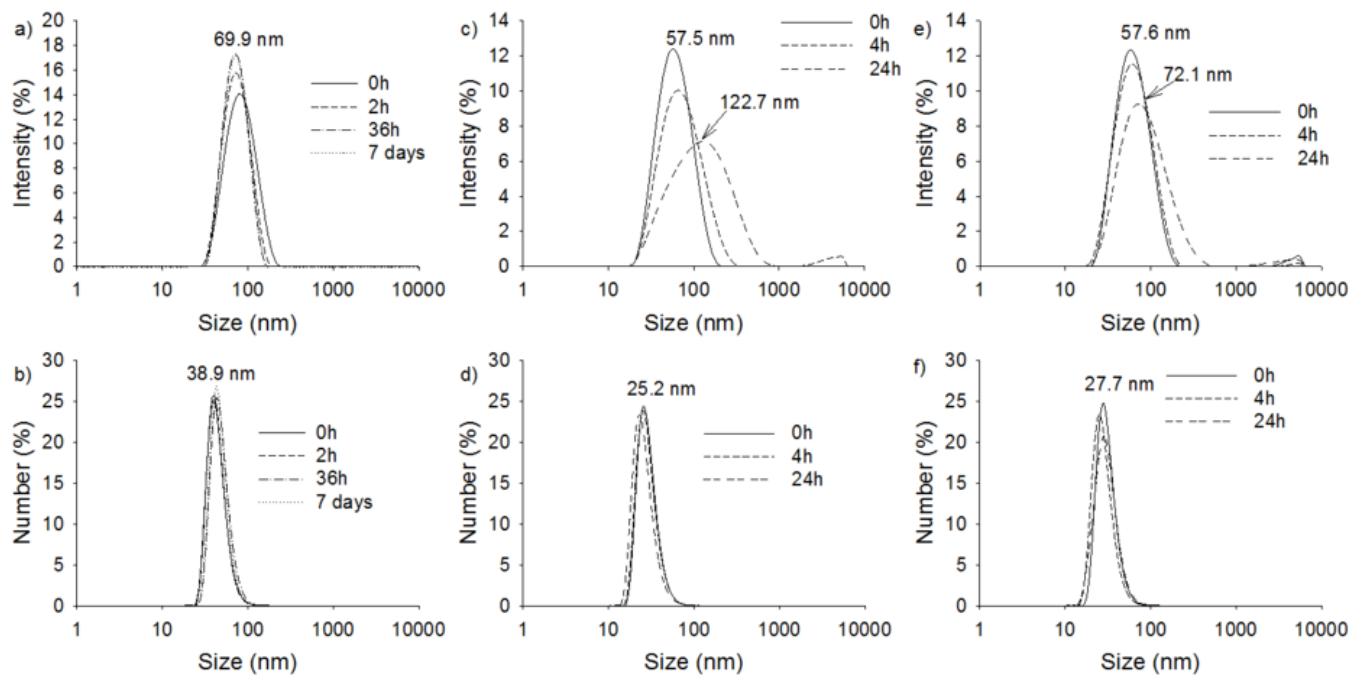

Fig. 8 Colloidal stability of Pd@Au-PEG in 154 mM NaCl (a-b), in DMEM for 2% v/v (c-d) and for 10% Pd@Au-PEG (e-f).

3.8: *In vitro* cell toxicity studies

The *in vitro* cell viability and proliferation assay was performed at Pd@Au-PEG NPs concentrations facilitating safe and exact pipetting of the fluid (not too viscous). In fact, solutions containing local concentrations of 5 mg Au NPs/g, or ~25 mM Au (suggested in [24]) imply the use of such high concentrations of Au-PEG NPs that the fluid becomes too viscous. Very high concentrations of Au NPs injected locally, might also cause complications due to normal inflammatory responses.

In the present study, the viability of PC3 cells was not affected by a 24-h treatment with Pd@Au-PEG NPs, up to a concentration of 4.22 mM (Fig.9). At the highest concentration, an inflexion was noted on both the viability results (~60%) and the cell proliferation (~40%; normalized to untreated controls). These results indicate that direct treatment of PC3 cells with high concentrations of Pd@Au-PEG NPs is likely to affect both the viability and the cell proliferation. This result can most probably be attributed to the large concentration of NPs internalised in the cells. Positive surface charge on these amine-containing NPs certainly influences the binding of NPs to membranes and, in turn, cell metabolism and duplication rate. Thus, the attachment of these NPs at the cellular membranes (cytosolic as well as endosomal), and their strong accumulation in the vesicles, may therefore contribute to the inhibition of the cell proliferation.

These cells were treated with non-radioactive NPs, and therefore the cytotoxicity effect most likely occurs from a combination of the following three factors: the presence of a high concentration of PEG as a nanoparticle surface ligand, inducing significant changes to the viscosity of DMEM; the large presence of residual $-SH$ and $-NH_2$ functions at the surface of Pd@Au-PEG NPs, which bind, interact with the cell membranes, and promote high internalisation of NPs; the possible presence of residual chlorides (from the metal precursors). The latter factor could be relatively easily controlled. However, PEG remain essential to the colloidal stability of Au NPs, and surface functions $-SH$ and NH_2, are essential to the synthesis, the colloidal stability, and the functionalization of Pd@Au NPs with functional molecules.

In order to attenuate the cytotoxic impact of Pd@Au-PEG NPs on the viability of prostate cells in future brachytherapy treatments, other approaches than direct injection of Au NPs into the tumours, must be considered. One promising alternative is the encapsulation of Pd@Au-PEG NPs into small (sub-millimetric) seeds made of highly biocompatible and biodegradable polymers. Polymer-encapsulated Pd@Au-PEG NPs could thereby be inserted as a new variety of brachytherapy implants, and progressively (in a matter of several weeks) elute Pd@Au-PEG NPs. The cytotoxicity effects caused to prostate cells could be better controlled, while enabling the progressive elimination of Au NPs from the site of implantations (over weeks).
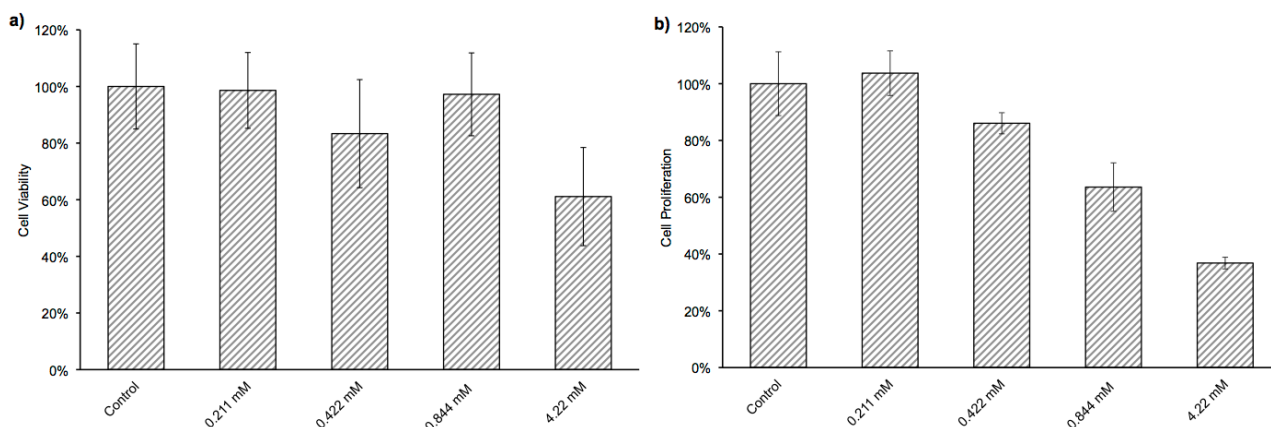

Fig. 9 Trypan blue cell viability assay (a) and SRB cell proliferation assay of PC3 cells incubated with Pd@Au-PEG NPs (b).

3.9 CT imaging

Au NPs are very efficient CT contrast agents. [57-60] In fact, the photoelectric effect depends on the atomic number of the atom (~Z^4) and on the energy of irradiating photons. Due to their high atomic number (Z = 79) and density, gold has a stronger X-ray absorption coefficient than iodine (Z = 53). As an example, the photon mass attenuation constant for Au at 100 keV is 5.16 cm^2g^{-1}, whereas that of iodine is 1.94 cm^2g^{-1} and that of bone 0.186 cm^2g^{-1}. [61] In this study, the X-ray attenuation properties of Pd@Au-PEG NPs were compared to that of AuroVist[TM] (15 nm), a commercial CT contrast agent. Fig. 10 shows the cross-section of contrast agent tubes imaged

by CT at different energies, with corresponding plots of X-ray attenuation as a function of concentration. Higher attenuation efficiency was found for Pd@Au-PEG NPs, at all scanning energies. This can be explained by the presence of small amounts of Pd in Pd@Au NPs (Pd: Au in a mass ratio of 1:29, or in a molar ratio of 1:15.5; confirmed by AAS measurements). With an attenuation coefficient of 16.1 cm^{2}g^{-1} for Pd, instead of 12.9 cm^{2}g^{-1} for Au (at 40 kV), Pd significantly contributes to the attenuation of X-rays. [61]
The impact of Au and Pd attenuation on X-ray attenuation, was measured from CT images, and plotted in Fig. 10b).

3.10: ^{103}Pd@Au-PEG NPs synthesis and imaging

The possibility to synthesize ^{103}Pd:Pd@Au-PEG rapidly was demonstrated in the course of this study. The synthesis of ^{103}Pd:Pd cores is estimated to 30 minutes when using multiple reaction volumes; coating with Au is instantaneous, whereas the PEG addition requires about 2 hours to make sure of an optimal binding of –SH groups with Au surfaces. The final centrifugation-wash cycles account for 45 minutes in total. Overall, the synthesis procedure for ^{103}Pd:Pd@Au-PEG can be performed in 4h.

As mentioned in section 2.4, an initial activity of 21 mCi was used to synthesize ^{103}Pd:Pd NPs. After Au coating, PEG grafting, followed by a first centrifugation cycle, the total activity present in the supernatant was 2.17 mCi (10.3% of the initial activity). The fraction of "free" ^{103}Pd correlates well with the >87% Pd reaction yield reported for "cold" Pd NP syntheses (section 3.2). The particles were suspended in nanopure water (1:20 volume ratio), and centrifuged again. The second supernatant from this wash-centrifugation cycle contained 254 µCi (1.2% of the initial activity). This procedure was repeated, and the third supernatant contained 19.9 µCi (0.09%). Finally, an ultimate centrifugation procedure was performed to re-concentrate the nanoparticles further: 1) the 4- mL NP suspension was centrifuged (supernatant: 1.29 µCi), followed by 2) a final centrifugation cycle (all at 16000g, 15 min.). This time, the very dense and viscous product was collected (125µL) and radioactivity-counted (274 µCi). Because the suspension was too dense to be easily pipetted, the final volume was adjusted with nanopure water to 600 µL (1.47 mCi; 304 mM

Au). Dilutions of this solution (5, 2, 1, 0,5 % v/v; 15.2, 5.1, 2.0, 1.0 mM Au) were pipetted in vials, and imaged in CT and SPECT (Fig. 10.a, lower insert). Finally, the empty tubes of all the synthesis/washing procedure were counted, indicating a total activity of 756 µCi (4.8% of the initial activity of 21 mCi).

The concentration-dependant photon attenuation effect of gold is clearly revealed in such results. Indeed, the activity of the final product (125µL; 274 µCi) increased by a factor of 5.36 after dilution to 600 µL (1.47 mCi). The exact same content of ^{103}Pd:Pd@Au-PEG was present in both vials, but not at the same concentrations. The mass attenuation coefficient of gold is 78.83 cm^{2}g^{-1} for the 20 keV photons emitted by ^{103}Pd. Taking into account the amount of 288 and 60 mg Au/mL (estimated both samples, respectively), linear attenuation coefficients as high as 22.7 cm^{-1} and 4.72 cm^{-1} are found. The photon attenuation effect of gold largely explains why, from a predicted final activity of ~ 17.83 mCi (21.0 − 2.17 − 0.25 − 0.75 − 0.0199 mCi = 17.81 mCi; 84.9% of the initial activity), a final measured activity of 1.47 mCi was found in the ^{103}Pd:Pd@Au-PEG aliquot.

The 10-20 nm-thick gold shell around the ^{103}Pd:Pd cores, is too thin to "block" the 20 keV photons emitted from the central radioactive core. The macroscopic attenuation effect is rather caused by the presence of a high concentration of Au in the vicinity of each emitting ^{103}Pd:Pd@Au-PEG NP. It is, indeed, a macroscopic shielding effect that significantly decreases when diluting the concentrated Au NPs solutions. Optimizing the balance between ^{103}Pd:Pd core activity, gold concentration, and macroscopic photon attenuation effect, is a priority in the perspective of studying ^{103}Pd@Au NPs impact on prostate cancer cells.
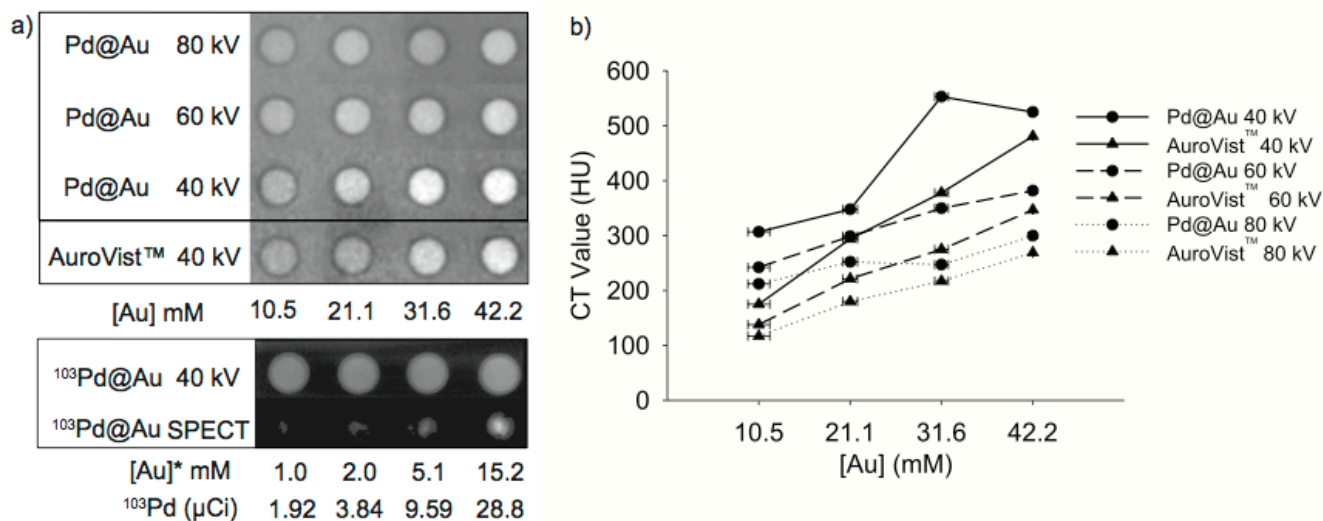
Fig. 10 Transverse CT images of Pd@Au-PEG NPs-containing tubes at different energies (a) and corresponding X-ray attenuation plots, as a function of gold concentration (b). * The Au concentration in [103]Pd:Pd@Au-PEG was estimated from a correlation curve obtained from the X-ray attenuation of Aurovist samples (at 40 keV).

4   Conclusions

This study reports a rapid (less than 4 hours), straightforward (1 step) and efficient way (> 85% reaction yield) to obtain Pd and Pd@Au-PEG NPs in aqueous media, and by using biocompatible molecules. In this one-pot, three-step process, ultra-small Pd NPs (diameter: 9.3 nm) were first synthesised, then coated with gold shells (total mean diameter: 20.2 nm) and functionalised with PEG. High reaction yields were achieved for the conversion of Pd salts into NPs. The core-shell nature of the nanoparticles was confirmed by HRTEM, EDX and XPS. Thus-obtained NPs formed very stable colloids in both saline and cell-culture media. The viability of PC3 prostate cancer cells treated 24 h, was not affected up to a concentration of 4.22 mM Au. The contrast-enhancement potential of Pd@Au-PEG NPs in CT imaging was higher than that of commercial Au-based CT contrast agents. This synthesis route enable the efficient production of radioactive [103]Pd:Pd@Au NPs, which could allow the generation of radiotherapeutic procedures, based on injections of radioactive and radiosensitising media, in the form of radioactive, Au-based NPs.

Notes and references

[a]Centre de recherche du Centre hospitalier universitaire de Québec (CR-CHUQ), axe Médecine Régénératrice, QC Québec, G1L 3L5, Canada
[b]Centre de recherche sur les matériaux avancés (CERMA), Université Laval, Québec, G1V 0A6, Canada
[c]Département de génie des mines, de la métallurgie et des matériaux, Université Laval, QC Québec, G1V 0A6, Canada
*Corresponding author: marc-andre.fortin@gmn.ulaval.ca, Phone: 1-418-525-4444 ext: 52366; Fax: 1-418-525-4372

1. G. Koukourakis, N. Kelekis, V. Armonis and V. Kouloulias, *Advances in urology*, 2009, 327945.

2. C. Polgar and T. Major, *International journal of clinical oncology*, 2009, **14**, 7-24.

3. J. P. Pignol, B. Keller, E. Rakovitch, R. Sankreacha, H. Easton and W. Que, *International journal of radiation oncology, biology, physics*, 2006, **64**, 176-181.

4. M. G. Dicker AP, Waterman FM, Valicenti RK, Gomella LG, *Basic and Advanced Techniques in Prostate Brachytherapy*, Martin Dunitz, Taylor and Francis Group, Abingdon (UK), 2005.

5. S. Jain, D. G. Hirst and J. M. O'Sullivan, *The British journal of radiology*, 2012, **85**, 101-113.

6. A. Nel, T. Xia, L. Mädler and N. Li, *Science*, 2006, **311**, 622-627.

7. P. Wust, B. Hildebrandt, G. Sreenivasa, B. Rau, J. Gellermann, H. Riess, R. Felix and P. M. Schlag, *The Lancet Oncology*, 2002, **3**, 487-497.

8. J. F. Hainfeld, D. N. Slatkin and H. M. Smilowitz, *Physics in medicine and biology*, 2004, **49**, N309-315.

9. D. M. Herold, I. J. Das, C. C. Stobbe, R. V. Iyer and J. D. Chapman, *International journal of radiation biology*, 2000, **76**, 1357-1364.

10. A. K. Pradhan, S. N. Nahar, M. Montenegro, Y. Yu, H. L. Zhang, C. Sur, M. Mrozik and R. M. Pitzer, *J Phys Chem A*, 2009, **113**, 12356-12363.

11. J. F. Hainfeld, F. A. Dilmanian, D. N. Slatkin and H. M. Smilowitz, *The Journal of pharmacy and pharmacology*, 2008, **60**, 977-985.

12. J. F. Hainfeld, F. A. Dilmanian, Z. Zhong, D. N. Slatkin, J. A. Kalef-Ezra and H. M. Smilowitz, *Physics in medicine and biology*, 2010, **55**, 3045-3059.

13. K. T. Butterworth, S. J. McMahon, F. J. Currell and K. M. Prise, *Nanoscale*, 2012, **4**, 4830-4838.

14. J. D. Carter, N. N. Cheng, Y. Qu, G. D. Suarez and T. Guo, *The journal of physical chemistry. B*, 2007, **111**, 11622-11625.

15. E. A. Foley, J. D. Carter, F. Shan and T. Guo, *Chem Commun (Camb)*, 2005, 3192-3194.

16. S. H. Cho, *Phys Med Biol*, 2005, **50**, N163-173.

17. W. N. Rahman, N. Bishara, T. Ackerly, C. F. He, P. Jackson, C. Wong, R. Davidson and M. Geso, *Nanomedicine : nanotechnology, biology, and medicine*, 2009, **5**, 136-142.

18. H. M. Garnica-Garza, *Phys Med Biol*, 2009, **54**, 5411-5425.

19. E. Brun, L. Sanche and C. Sicard-Roselli, *Colloid Surface B*, 2009, **72**, 128-134.

20. S. H. Cho, B. L. Jones and S. Krishnan, *Phys Med Biol*, 2009, **54**, 4889-4905.

21. M. K. Leung, J. C. Chow, B. D. Chithrani, M. J. Lee, B. Oms and D. A. Jaffray, *Medical physics*, 2011, **38**, 624-631.

22. M. Montenegro, S. N. Nahar, A. K. Pradhan, K. Huang and Y. Yu, *J Phys Chem A*, 2009, **113**, 12364-12369.

23. B. L. Jones, S. Krishnan and S. H. Cho, *Medical physics*, 2010, **37**, 3809-3816.

24. E. Lechtman, N. Chattopadhyay, Z. Cai, S. Mashouf, R. Reilly and J. P. Pignol, *Phys Med Biol*, 2011, **56**, 4631-4647.

25. W. Ngwa, H. Korideck, A. I. Kassis, R. Kumar, S. Sridhar, G. M. Makrigiorgos and R. A. Cormack, *Nanomed-Nanotechnol*, 2013, **9**, 25-27.

26. K. Canxia, C. Weiping, L. Cuncheng, Z. Lide and H. Hofmeister, *Journal of Physics D: Applied Physics*, 2003, **36**, 1609.

27. V. Mazumder, M. Chi, K. L. More and S. Sun, *Angewandte Chemie International Edition*, 2010, **49**, 9368-9372.

28. J. Liu, F. He, T. M. Gunn, D. Zhao and C. B. Roberts, *Langmuir*, 2009, **25**, 7116-7128.

29. Y. Piao, Y. Jang, M. Shokouhimehr, I. S. Lee and T. Hyeon, *Small*, 2007, **3**, 255-260.

30. S. Sharma, B. Kim and D. Lee, *Langmuir*, 2012, **28**, 15958-15965.

31. P. Zhao, N. Li and D. Astruc, *Coordination Chemistry Reviews*, 2013, **257**, 638-665.

32. B. Lim, H. Kobayashi, T. Yu, J. Wang, M. J. Kim, Z.-Y. Li, M. Rycenga and Y. Xia, *Journal of the American Chemical Society*, 2010, **132**, 2506-2507.

33. C. J. DeSantis and S. E. Skrabalak, *Journal of the American Chemical Society*, 2012, **135**, 10-13.

34. J. C. C. J. Serpell, D. Ozkaya and P. D. Beer, *Nature Chemistry*, 2011, **3**, 478-483.

35. S. Arora, M. L. Singla and P. Kapoor, *Materials Chemistry and Physics*, 2009, **114**, 107-112.

36. Y. Xiong, J. Chen, B. Wiley, Y. Xia, S. Aloni and Y. Yin, *Journal of the American Chemical Society*, 2005, **127**, 7332-7333.

37. S.-W. Kim, J. Park, Y. Jang, Y. Chung, S. Hwang, T. Hyeon and Y. W. Kim, *Nano Letters*, 2003, **3**, 1289-1291.

38. Y. Shi, S. Yin, Y. Ma, D. Lu, Y. Chen, Y. Tang and T. Lu, *Journal of Power Sources*, 2014, **246**, 356-360.

39. S. U. Son, Y. Jang, K. Y. Yoon, E. Kang and T. Hyeon, *Nano Letters*, 2004, **4**, 1147-1151.

40. Z. Yang and K. J. Klabunde, *Journal of Organometallic Chemistry*, 2009, **694**, 1016-1021.

41. M. Cargnello, N. L. Wieder, P. Canton, T. Montini, G. Giambastiani, A. Benedetti, R. J. Gorte and P. Fornasiero, *Chemistry of Materials*, 2011, **23**, 3961-3969.

42. Liu, F. He, E. Durham, D. Zhao and C. B. Roberts, *Langmuir*, 2007, **24**, 328-336.

43. Z. Zhao, Y.-L. Fang, P. J. J. Alvarez and M. S. Wong, *Applied Catalysis B: Environmental*, 2013, **140–141**, 468-477.

44. L. Wu, B.-L. Li, Y.-Y. Huang, H.-F. Zhou, Y.-M. He and Q.-H. Fan, *Organic Letters*, 2006, **8**, 3605-3608.

45. Z. Wang, H. Li, S. Zhen and N. He, *Nanoscale*, 2012, **4**, 3536-3542.

46. L.-M. Lu, H.-B. Li, F. Qu, X.-B. Zhang, G.-L. Shen and R.-Q. Yu, *Biosensors and Bioelectronics*, 2011, **26**, 3500-3504.

47. T. Teranishi and M. Miyake, *Chemistry of Materials*, 1998, **10**, 594-600.

48. C. J. DeSantis, A. C. Sue, M. M. Bower and S. E. Skrabalak, *ACS Nano*, 2012, **6**, 2617-2628.

49. M. Luty-Błocho, K. Pacławski, M. Wojnicki and K. Fitzner, *Inorganica Chimica Acta*, 2013, **395**, 189-196.

50. C. J. Murphy, A. M. Gole, S. E. Hunyadi and C. J. Orendorff, *Inorganic Chemistry*, 2006, **45**, 7544-7554.

51. G. B. Deacon, F. Huber and R. J. Phillips, *Inorganica Chimica Acta*, 1985, **104**, 41-45.

52. G. B. Deacon and R. J. Phillips, *Coordination Chemistry Reviews*, 1980, **33**, 227-250.

53. A. Zhang, M. Liu, M. Liu, Y. Xiao, Z. Li, J. Chen, Y. Sun, J. Zhao, S. Fang, D. Jia and F. Li, *Journal of Materials Chemistry A*, 2014, **2**, 1369-1374.

54. J. Zhou, C. Soto, M.-S. Chen, M. Bruckman, M. Moore, E. Barry, B. Ratna, P. Pehrsson, B. Spies and T. Confer, *Journal of Nanobiotechnology*, 2012, **10**, 18.

55. M. Brun, A. Berthet and J. Bertolini, *J Electro Spec Rel Phe*, 1999, **104**, 55 - 60.

56. M. Letourneau, M. Tremblay, L. Faucher, D. Rojas, P. Chevallier, Y. Gossuin, J. Lagueux and M. A. Fortin, *The journal of physical chemistry. B*, 2012, **116**, 13228-13238.

57. J. F. Hainfeld, D. N. Slatkin, T. M. Focella and H. M. Smilowitz, *The British journal of radiology*, 2006, **79**, 248-253.

58. N. Lee, S. H. Choi and T. Hyeon, *Advanced Materials*, 2013, **25**, 2641-2660.

59. R. Popovtzer, A. Agrawal, N. A. Kotov, A. Popovtzer, J. Balter, T. E. Carey and R. Kopelman, *Nano Letters*, 2008, **8**, 4593-4596.

60. L. Nebuloni, G. A. Kuhn and R. Müller, *Academic Radiology*, 2013, **20**, 1247-1255.

61. National Institute of Standards and Technology, http://www.nist.gov/pml/data/xraycoef, Accessed 16/07/2014, 2014.